Journal of Cultural Heritage 71 (2025) 320–327

Contents lists available at ScienceDirect

Journal of Cultural Heritage

journal homepage: www.elsevier.com/locate/culher

VSI: TechnoHeritage2024

Color reconstruction by photometric stereo with unknown lighting of rock art carvings found in two Sardinian *Domus de Janas*

Elisa Crabu[a,*], Federica Pes[a], Giuseppe Rodriguez[a], Giuseppa Tanda[b]

[a] Department of Mathematics and Computer Science, University of Cagliari, Cagliari, 09124, Italy
[b] CeSim - Centro Studi "Identità e Memoria", Sassari, 07100, Italy

ARTICLE INFO

Article history:
Received 4 July 2024
Revised 27 November 2024
Accepted 19 December 2024

Keywords:
Photometric stereo
Shape from shading
Rock art carvings

ABSTRACT

Artifacts documentation is an important aspect of archaeological studies, not only to preserve these objects but also to learn from them the culture of ancient populations. Hence, the necessity to digitally document and archive artifacts that come from our ancestors. This work can be done with more ease for artifacts as vases, potsherds, or little handmade objects, that can be brought in a laboratory. It is more complicate for rock art carvings, that can not be moved from their original location. The photometric stereo technique allows to obtain the three-dimensional digital reconstruction of an object starting from a set of pictures taken with different lighting conditions. When the method is applied to some experimental datasets, computational problems may occur, due to the fact that some assumptions of the model are not verified: rocks are not Lambertian surfaces in general, and the light sources may not be positioned at a sufficient distance from the object. We deal with these issues by introducing numerical indicators of ideality that allow to figure out if a given dataset is reliable and which images should be selected to better reproduce the object. In this paper, we will show the application of this method to the 3D reconstruction of some engravings found in two *Domus de Janas*, ancient tombs located in Sardinia, Italy.

1. Introduction

Knowledge of traditions and rituals of ancient populations goes through the study of archaeological artifacts, whose documentation turns out to be of primary interest for archaeologists. In classical cataloguing, artifacts are removed from their original location and placed in protected environments to reduce their deterioration. For architectural findings, the conservation is different: they can not be removed, so the archaeological intervention is done with the perspective of in-site maintenance. In this case, the main issue is that they suffer the action of weather elements, such as wind or rain, which lead to a continuous deterioration.

Our area of interest is connected with burial rituals of the prenuragic period in Sardinia. Funerary rituals had a profound significance for ancient civilizations. They are representative of the culture and their studies allow to learn the history of populations. In Sardinia, the dead cult in the Neolithic period found its representation in *Domus de Janas*, funerary hypogea that have been the central location of these rituals [1]. They are formed by rooms, carved into the rock, many of which are decorated with art motifs. In this culture, art motifs are an important aspect of the funerary customs, as a part of propitiation rites of the souls of the deceased and their divinities. They are executed with different techniques (sculpture, painting, and engravings) and their location inside the environments has varied over the time. There are many types of motifs, representing horn-shape, anthropomorphic, and geometric figures, as in Fig. 1.

Due to the fact that these sites are not safeguarded, atmospheric agents are slowly deteriorating the engravings. This is a huge problem for the preservation of this heritage and it is desirable to be able to digitally document these artifacts with accuracy, both to secure at least a digital copy for future generations and to be able to examine the carved surfaces on a graphic workstation without further contact with the original artifacts.

Photometric stereo (PS) [2] is a computer vision technique that provides a digital reconstruction of an object, extracting shape and color information from digital pictures obtained under different lighting conditions. It has been repeatedly applied in the past to the documentation of rock art; see [3,4] for a previous application to the *Domus de Janas* sites.

* Corresponding author.
E-mail addresses: elisa.crabu@unica.it (E. Crabu), federica.pes@unica.it (F. Pes), rodriguez@unica.it (G. Rodriguez), giuseppa.tanda@gmail.com (G. Tanda).

https://doi.org/10.1016/j.culher.2024.12.019

Fig. 1. Two examples of geometric and anthropomorphic figures, found in *Domus de Janas di Corongiu*, Pimentel (top picture) and *Domus de Janas di Tomba Branca*, Cheremule (bottom picture), both in Sardinia, Italy.

Many other related works can be found in the literature. In [5], a software that combine PS and photogrammetry has been developed for the 3D digitization of cultural heritage, while in [6] a study of rock art carvings of two Iberian stelae has been carried out by a RTI approach. A novel PS method has been applied in [7] to reconstruct a cultural asset called Segonko Tumulus, whose walls are carved and painted. Finally, in [8] a digitalization of decorative tumuli in Kyushu (Japan), which present mural paintings, has been studied using photometric approaches.

In the standard configuration of the PS model, the camera is positioned in front of the observed surface and a light source is placed at different positions with respect to it, so that each image of the dataset corresponds to different illumination conditions. The mathematical model assumes that the camera is placed "at infinite distance" from the object (orthographic projection) as well as the light sources, i.e., the light rays can be considered parallel. Moreover, the surface is assumed to be a Lambertian reflector: it diffuses the light in the same way in each direction, that is, the reflected light intensity is the same from any point of view.

While in our experimentation a simple flashlight was used as a light source, different choice for the light source can be made: in [9] an experimental dataset was obtained using the sun as a light source, to ensure parallel light rays; in [10] diods as point light sources illumination have been used to present a LED-based PS method.

In the original setting, the lights position are considered known before data processing. This condition is a strong limitation in real applications, in particular in archaeological ones. Indeed, it is generally impossible to exactly measure the position of light sources during the acquisition of the images. The uncalibrated PS has been addressed in different ways: in [11] a patch-based approach has been considered, while in [12] and [13] two networks have been developed to treat the problem. A different approach has been proposed by Hayakawa, who introduced in [14] a method to estimate light position information directly from the data, with the assumption that the dataset is composed of at least six images.

Although the method performs efficiently on synthetic datasets, its application to experimental datasets leads to numerous computational problems. Indeed, data processing clearly shows that many datasets lack "ideality", in the sense that, due to the fact that some of the assumptions of the model are not met, the results may be inaccurate or algorithmic *breakdowns* verify unexpectedly. This happens because the structure of the sites and the materials of which the artifacts are made, often do not permit to completely satisfy the model assumptions. For example, given the small scale of *Domus de Janas*, it is usual impossible to place the light source at a sufficient distance from the surface, to produce approximately parallel light rays. Moreover, rock is generally far from being an ideal Lambertian reflector; for a preprocessing approach to partially recover lack of Lambertianity, see [15].

Different studies have been devoted to the non Lambertian case. In [16], using a Bayesian approach, a statistical method based on the resolution of a sparse regression problem was solved to determine an approximation of the normal vector field and the experimental errors. Various learning-based algorithms were used to solve the non Lambertian PS problem, see, e.g., [17,18]. The approach presented in [19], starting from the observation that non Lambertian surfaces are subject to shadows and specular reflections, considers a solution method based on a low-rank matrix factorization affected by sparse errors. In general, various methods have been considered to remove outliers from a dataset, as it happens in the case of specular reflections, like L_p-norm regularization with $p < 2$, robust SVD, etc. Such methods are not applicable in our case since the lack of ideality present in the dataset we consider is not due to the presence of outliers.

A solution explored in [20], which assumes that the surface is only approximately Lambertian, is to extract from a dataset a subset of images that produces the best possible reconstruction of the observation, trying to approximately satisfy as much as possible the strict assumptions of the model. Two indicators were proposed to allow the identification of a subset that produces an accurate three-dimensional shape reconstruction, and were tested on synthetic datasets, showing their effectiveness.

In this paper, we describe an approach for dealing with color datasets and apply it to the reconstruction of various engravings found in Sardinian *Domus de Janas*. Initially, we briefly review the main steps of the photometric stereo method, debating also the problems connected with real shooting conditions, and then we consider its application to experimental datasets of rock art carvings.

Various papers has been devoted to photometric stereo with color images. One of the first to appear was [21]. In [22], the authors propose a method to estimate shape and color information using three colored images, which are the best with respect to a least-squares approach. An iterative procedure based on the Jabobi method was presented in [23]. In the interesting procedure analyzed in [24], the observed surface is illuminated by differently colored light sources.

2. Research aim

Elaboration of color datasets are of crucial importance in photometric stereo. Indeed, most cameras capture by default color images, which are often converted to grayscale images after data acquisition. Each color image is actually composed of three images, each one containing the contribution of each primary color, namely, red, green, and blue. Hence, the acronym RGB used for this kind of images.

Theoretically, each color channel should be able to reconstruct the shape of the observed object by applying the photometric

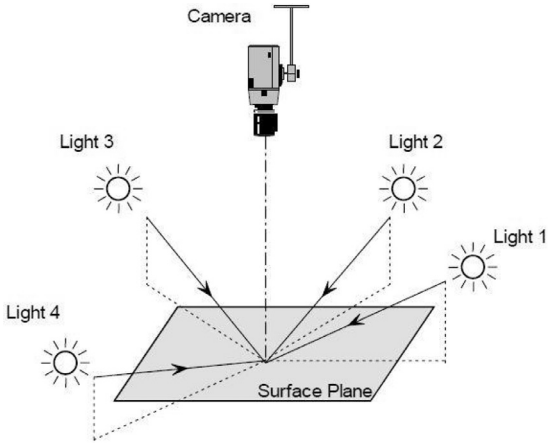

Fig. 2. Configuration of the system.

stereo technique. In practice, it may happen that one of the color channels contains degraded information, due to chromatic features of the observation or to malfunctioning of the camera sensor. This aspect is discussed in Section 4, where a numerical test on a synthetic dataset is illustrated.

Our main concern in this paper is to determine a procedure to automatically select in a dataset the color channel which is more suitable to obtain a faithful shape reconstruction of the observation, and then complete the chromatic information by using the two remaining channels.

3. Methods

Here, we briefly describe the mathematical tools used in the numerical experiments.

3.1. Photometric stereo with unknown lighting

Photometric stereo [2] is a Shape from Shading technique that extracts from a set of images of the target enough information to digitally reconstruct its shape. The model has been much studied in the past, in this section we will recap its application.

The configuration of the system, illustrated in Fig. 2, places the camera at a fixed position in front of the object to be recovered. Images are collected by placing the light source at different positions around the target, so that the dataset consists of a set of pictures obtained under distinct lighting directions. Theoretically, both the camera and the light source should be placed at infinite distance from the target. In practice, they are both positioned as far as possible from it.

The object is assumed to be at the origin of an orthonormal reference system in $\mathbb{R}^3$, and the camera is such that its optical axis coincides with z-axis of the system.

Let $z = u(x, y)$, $(x, y) \in \Omega$ (the observed domain), be the bivariate function that represents the surface of the target, with u_x, u_y its partial derivatives, and let $\mathbf{n}(x, y)$ be the normalized normal vector.

The finite resolution of a digital camera induces a discretization of the domain Ω, i.e., a grid of points with coordinates (x_i, y_j), $i = 0, \dots, r+1$, $j = 0, \dots, s+1$. By evaluating functions on the grid and lexicographically ordering the points, that is, column by column, we indifferently indicate the value of u on a grid point by $u(x_i, y_j)$, $u_{i,j}$, or u_k, where $k = (i-1)s + j$, for $k = 1, \dots, p$,

The standard model for photometric stereo assumes that the surface of the target is a Lambertian reflector, that is, it satisfies *Lambert's cosine law*:

$$\rho(x, y)\langle \mathbf{n}(x, y), \boldsymbol{\ell}_t \rangle = I_t(x, y), \qquad t = 1, \dots, q, \tag{1}$$

where $\langle \cdot, \cdot \rangle$ denotes the usual scalar product in $\mathbb{R}^3$ and $\boldsymbol{\ell}_t = [\ell_{1t}, \ell_{2t}, \ell_{3t}]^T$ is the vector oriented from the target to the light source, whose norm is proportional to the light intensity. The function $\rho(x, y)$ is the *albedo*, which takes into account the partial absorption of the light from the surface, and $I_t(x, y)$ is the radiation intensity of the tth image, that is, the value measured by the camera sensor. Here, we assume to deal with a grayscale image or with the contribution of a single color channel.

In this paper we consider the length of the light vectors $\boldsymbol{\ell}_t$ to be constant, that is, the illumination has the same intensity in each frame. This assumption is approximately verified in practice, as during shooting we try to keep the flashlight approximately at the same distance from the observed surface. Whenever this is not possible, one may estimate the relative length of the light vectors by taking incident light metering measures at shooting time. This is allowed by any professional light meter.

By discretizing formula (1) and applying the lexicographic ordering, we obtain the matrix equation

$$DN^T L = M, \tag{2}$$

where $D = diag(\rho_1, \dots, \rho_p)$ contains the values of the albedo at each of the p grid points, $N = [\mathbf{n}_1, \dots, \mathbf{n}_p]$ the corresponding normal vectors, and $L = [\boldsymbol{\ell}_1, \dots, \boldsymbol{\ell}_q]$ the light directions adopted in the q available images. The matrix $M = [\mathbf{m}_1, \dots, \mathbf{m}_q]$ represents the dataset: each column contains a vectorized digital image.

Under the assumption of known light source positions, the matrix L is available. In this case the problem can be easily solved; see [9]. Once the discretized field of normal vectors is determined, the object surface can be obtained by integrating a system of Hamilton-Jacobi partial differential equations or by solving a Poisson problem $\Delta u(x, y) = f(x, y)$; see, e.g., [9,25]. In the examples shown in this paper, for simplicity, we employed the Poisson technique by a classical 5 point integrations scheme. Since solving partial differential equations implies smoothness of the solution, such methods poorly handle discontinuities. Slightly better results might be obtained by resorting to bilateral integration techniques [26], which only require piecewise differentiability.

The request of known lighting is a huge limitation, especially in the archaeological application, where data are often acquired on field under uneasy conditions which may make it impossible to measure the exact positions of a light source during image acquisition. Hayakawa [14] determined a procedure to deal with unknown light source position, and proved that at least six images must be available to compute a reconstruction. Since this method assumes the Lambertianity of the observed surface, its applicability was used in [20] to assess the ideality of a dataset. To describe such ideality indicator, whose use is crucial in this paper, we review here the main steps of Hayakawa's method to estimate the position of light sources.

From the singular value decomposition [27] of the data matrix $M = U\Sigma V^T$, an initial factorization $M = W^T Z$ is obtained by setting $W = [\sigma_1 \mathbf{u}_1, \sigma_2 \mathbf{u}_2, \sigma_3 \mathbf{u}_3]^T$ and $Z = [\mathbf{v}_1, \mathbf{v}_2, \mathbf{v}_3]^T$, where σ_i are the singular values of M and $\mathbf{u}_i$, $\mathbf{v}_i$ its left and right singular vectors, respectively.

The second step of Hayakawa's procedure consists of seeking a matrix B that simultaneously normalizes the columns of Z, that is,

$$\|B\mathbf{z}_t\| = 1, \qquad t = 1, \dots, q. \tag{3}$$

This leads to the resolution of a system of q linear equations, each corresponding to an image in the dataset, whose 6 unknowns determine the positive definite matrix $G = B^T B$. The solution of the linear system is unique only if the system is overdetermined and full-rank, i.e., $q \geq 6$. The matrix B is computed from G by its Cholesky factorization [27].

To solve the so-called *bas-relief ambiguity* [28], caused by the uncertainty in the reference rotation, we adopt a method described

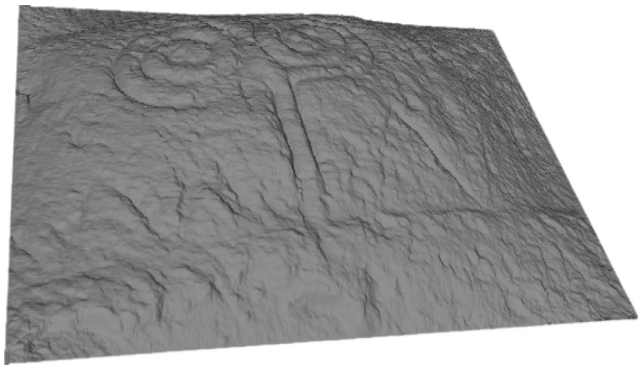

Fig. 3. An inaccurate reconstruction.

in [9], where a software implementation of Hayakawa procedure is also presented. This determines a rotation matrix Q. Since this part of the process is not relevant for this paper, we refer to [9] for further details. Once B and Q are known, the final factorization is obtained by setting $\tilde{N} := ND = QB^{-T}W$ and $L = QBZ$.

3.2. Ideal data

Hayakawa's method produces accurate reconstructions when the assumptions of model (1) are valid. Nevertheless, its application to experimental data often exhibits the occurrence of computational problems. In particular, the computed reconstruction may be inaccurate, or Hayakawa's algorithm may even interrupt with a run-time error.

In the first scenario, the reconstruction appears different from the real object because of an evident deformation, as in Fig. 3. When a breakdown of the algorithm occurs a reconstruction of the observed surface cannot even be computed. This happens when the matrix G, obtained by the Hayakawa procedure, turns out to be non-positive definite, contrarily to theoretical assumptions. Indeed, for some experimental datasets it may happen that the smallest eigenvalue of G is negative, leading to a breakdown in the computation of its Cholesky factor, which provides the matrix B.

These issues are attributable to distortion in available information, due to non-ideality of data. For particular experimental datasets, some theoretical conditions imposed by the model may not be satisfied. For example, *Domus de Janas* present engravings located inside small and narrow rooms, so neither the camera nor the light source can be placed far enough from the observed surface. Furthermore, the rock is not an ideal Lambertian reflector, and this makes the experimental environment further less compliant with the model. When Hayakawa's procedure is applied, this lack of ideality often leads to a non-positive definite matrix G.

In [20], two "ideality indicators" for a dataset were proposed. In the same paper, a method based on such indicators was introduced to extract from a non-ideal dataset a subset of images that approximately satisfies the assumption of the model.

The first approach consists of considering the success of Hayakawa's procedure as an ideality indicator for a collection of images. Since a bad dataset leads to a non-positive definite matrix G (see Section 3.1), the smallest eigenvalue of G is taken as a quality index. We denote this indicator by $\rho_1(M)$, where M is the image collection for which it is computed. If it is positive, the dataset is accepted, otherwise one image at a time is removed from the collection, choosing the configuration for which $\rho_1(M)$ takes the largest value. If the indicator for the reduced dataset is positive, it is accepted, otherwise the process is iterated until either the condition is verified or less than 6 images are left. This is considered a failure, since Hayakawa's method requires the availability of at least 6 images.

In [20], a new method for determining the lights position, alternative to Hayakawa's one, was proposed. It is based on the idea of solving (3) as a nonlinear least-squares problem

$$\min_{\mathbf{b}\in\mathbb{R}^6} \|F(\mathbf{b})\|^2, \tag{4}$$

where

$$F(\mathbf{b}) = [f_1(\mathbf{b}), \dots, f_q(\mathbf{b})]^T, \quad f_t(\mathbf{b}) = \|B\mathbf{z}_t\|^2 - 1,$$

and the vector $\mathbf{b}$ contains the six nonzero entries of the upper triangular matrix B. Since the Jacobian matrix $J(\mathbf{b})$ is analytically known, we minimize (4) by the Gauss–Newton algorithm [29], as implemented in [30,31]. For explicit expressions of $F(\mathbf{b})$ and its Jacobian, or other details about the implementation, see [20].

The second indicator $\rho_2(M)$ is connected to the use of the Gauss–Newton method to solve problem (4). It has been observed that the above method diverges in the presence of non-ideal images. Indeed, in such situation, the Jacobian matrix becomes rank deficient during iteration. Since $J(\mathbf{b})$ is a $q \times 6$ matrix, with $q \geq 6$, the indicator $\rho_2(M)$ has been defined as the ratio between its sixth and fifth singular values, so as to detect rank deficiency. Similarly to the previous approach, the initial dataset is accepted if $\rho_2(M)$ is significantly larger than zero. If this does not happen, an iterative method is constructed to remove images from the available collection in order to make the ratio $\rho_2(M)$ larger than a chosen threshold. The Matlab implementation of both indicators is available from the authors.

3.3. Color channels processing

A digital RGB color picture is composed of three matrices, one for each color channel. Let us denote the data matrices in (2) corresponding to red, green, and blue by M_r, M_g, and M_b, respectively. This leads to three matrix equations

$$D_\tau N_\tau^T L_\tau = M_\tau, \qquad \tau = r, g, b. \tag{5}$$

Applying Hayakawa's method to (5) produces three sets of solutions, each composed of a diagonal albedo matrix D_τ, and matrices N_τ and L_τ containing the normal vectors and the light directions, respectively.

Theoretically, the triplets (D_τ, N_τ, L_τ) containing the solution of (5) should differ only in the albedo matrix D_τ, while N_τ and L_τ should be independent of τ. In practice, the triplets are sensibly different also for good datasets, and can be dramatically different for non-ideal datasets, leading to inaccurate reconstructions.

Using grayscale images for reconstructing the shape of the surface, and the three Eq. (5) for obtaining its color, may be a solution but, when a particular color channel produces inaccurate data, the data inaccuracy propagates to the grayscale image. In this case it would be preferable to use the best color channel to reconstruct the shape, and the other two channels to complete the color information for the albedo.

Our approach, in this paper, is to apply either of our ideality indicators ρ_1 and ρ_2 to independently reduce the datasets for the three color channels, and then produce a ranking for the three channels based on the same indicator. To exemplify, we fix $k = 1, 2$ and consider the values

$$\rho_k(M_r), \quad \rho_k(M_g), \quad \rho_k(M_b),$$

and select the color channel with the more favorable indicator value. This means the smallest value for ρ_1, the largest one for ρ_2.

If, for example, the blue channel is selected, then (5) is first solved for $\tau = b$ and the normals N_b are used to reconstruct the shape of the observed surface, while D_b represents the blue contribution to the color of the object. Then, the same problem is solved for $\tau = r, g$ and the obtained albedos D_r and D_g complete the color information.

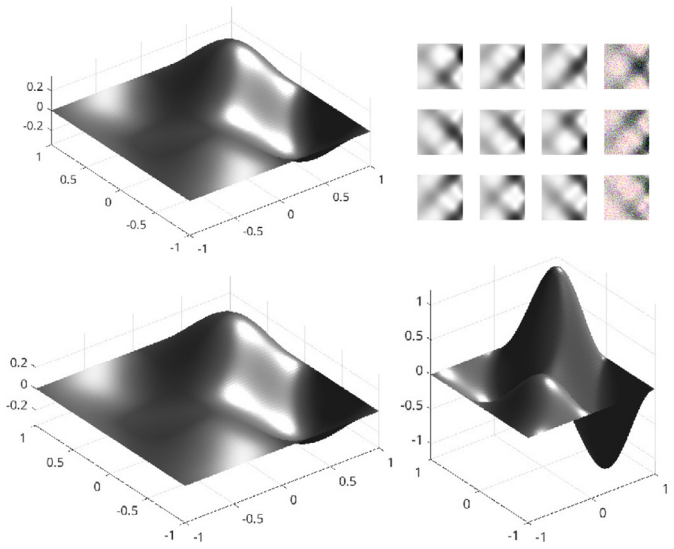

Fig. 4. The effect of noisy data channels: top left, model surface; top right, synthetic dataset with three images presenting noise in the green and blue channels; bottom left, shape reconstructed from the red channel; bottom right, reconstruction produced by the green channel.

An alternative approach, which is more time demanding, consists of converting the color images to grayscale and solve (2) to obtain the matrix N. Then, we select the color channel for which the value $\|N - N_\tau\|_1$ is the smallest.

4. Results

In this section, we present color reconstructions obtained by applying the approach described in Section 3.3. Starting from a collection of RGB images, we compute for each color matrix M_r, M_g, and M_b, one of the ideality indicator, either ρ_1 or ρ_2. Based on the values of the chosen indicator, we take the decision of selecting the color layer to be processed.

Before discussing the two experimental datasets which constitute the case study considered in this paper, we show the effect of the presence of data channels containing inaccurate data. We produced a synthetic dataset of 12 images from a model smooth surface, using the package described in [32]; see Fig. 4. The RGB albedo of the surface has been set to white, that is, each of the three color layer contains the same value. Then, Gaussian noise was added to the green and blue channels of three images in the dataset, and the surface was reconstructed by the Hayakawa procedure as implemented in [9], using a dataset restricted to each of the color channels. The reconstruction produced by the green channel is highly deformed with respect to the good approximation produced by the red one, as Fig. 4 shows. The reconstruction obtained by processing the blue channel is similar to the green one.

These results were obtained with 30% noise. In this case the indicator ρ_1 was able to identify the "clean" red color layer and to recognize the three noisy images in the dataset. Reducing the dataset according to this information does not produce accurate results, as the figure shows, but furnishes some information on the shape. The red layer was classified as the best one also by ρ_2, but this indicator was not able to select the three images to be removed. From the point of view of producing an accurate shape reconstruction, both indicators were successful, as their suggestion on the layer to be processed is correct.

If the noise level is lowered to 10%, the situation changes. Indeed, in this case ρ_1 is not able to recognize the noise-free red layer and leads to an inaccurate (even if acceptable) reconstruction. On the contrary, ρ_2 correctly identifies the red color plane and produces the best results. This shows that the two proposed indicators do not yield an automated procedure to select an ideal set of images from an available dataset, but they are both useful tools in a supervised selection process, especially because it is not possible to visually identify a subset of images which allows an effective PS processing.

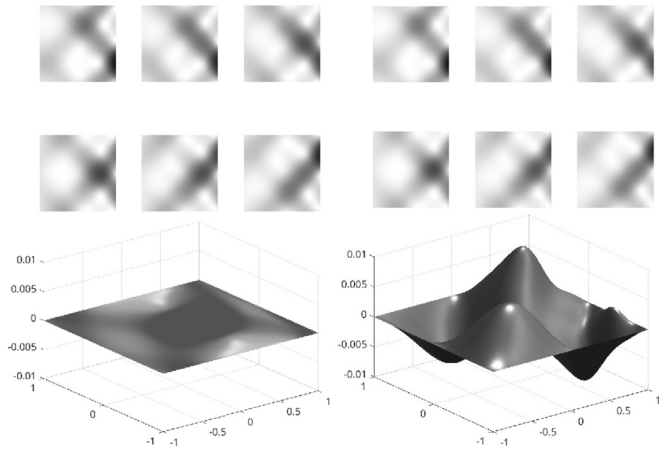

Fig. 5. The top rows displays the first six images of two grayscale datasets produced by the `rgb2gray` function of Matlab (left) and by the `rgb2lightness` function (right) starting from a RGB white surface. The bottom rows shows the error surfaces corresponding to the PS reconstructions of the two datasets.

As we already observed in Section 3.3, reconstruction from grayscale images is not always a good choice, since a bad color channel may distort the shape information in the converted images. We also remark that different grayscale conversion algorithms may produce sensibly different results. Indeed, even when the content of all the color channels is acceptable, not all RGB to grayscale conversion algorithms produce images suitable for photometric stereo. For example, Matlab provides two functions to perform this task. According to the manual, `rgb2gray` works by eliminating the hue and saturation information from the input image, retaining only the luminance. On the contrary, `rgb2lightness` converts RGB color values to lightness values, excluding the color components. We generated two grayscale datasets for the model surface displayed in Fig. 4, using the two above conversion functions. The graphs in the top row of Fig. 5 show that the two datasets are visually indistinguishable, but the reconstruction errors visualized in the bottom row demonstrate that the surface obtained from the dataset generated by `rgb2gray` is more accurate than the one corresponding to the `rgb2lightness` dataset.

We now illustrate this selection process on two experimental datasets concerning engravings found in two different *Domus de Janas*. The first one (see top picture in Fig. 1) is found in *Domus de Janas di Corongiu* (Pimentel, Italy). We collected 13 color pictures of it under different lighting conditions, 4 of them are displayed in Fig. 6.

The datasets corresponding to the three color channels are first reduced according to the technique introduced in [20], based on the ideality measure ρ_2. The values of the indicator ρ_2 for the reduced datasets are the following:

$$\rho_2(M_r) = 0.9609,$$
$$\rho_2(M_g) = 0.9646,$$
$$\rho_2(M_b) = 0.9918.$$

Since the blue channel corresponds to the largest value, we take the decision to employ the matrix M_b to compute the shape of the surface and the blue component of the albedo. The other

Fig. 6. Four of the 13 images from the first dataset, each obtained under different lighting conditions.

Fig. 7. Reconstruction of the first engraving obtained by the blue channel of the dataset: complete color reconstruction (top picture), normal map (center picture), and pure shape without the albedo (bottom picture).

two matrices are used to obtain the remaining color information. The resulting reconstruction, coupling the surface and the albedo, is displayed in the top picture of Fig. 7. The other two pictures exhibit the normal map, and the shape information obtained by removing the albedo.

To highlight the importance of the choice of the color channel, we display in the top picture of Fig. 8 the shape reconstruction obtained by processing the red channel, instead of the blue one. The deformation of the surface is evident, especially when compared to the blue one, reported in the center picture. The inaccuracy of the reconstruction is also highlighted by the normal map, displayed in the bottom picture. We do not display the colored surface because the computed albedo is completely wrong. We remark that the use of the first indicator ρ_1 leads to a failure, as it selects the red color layer, leading to the distorted reconstruction shown in Fig. 8.

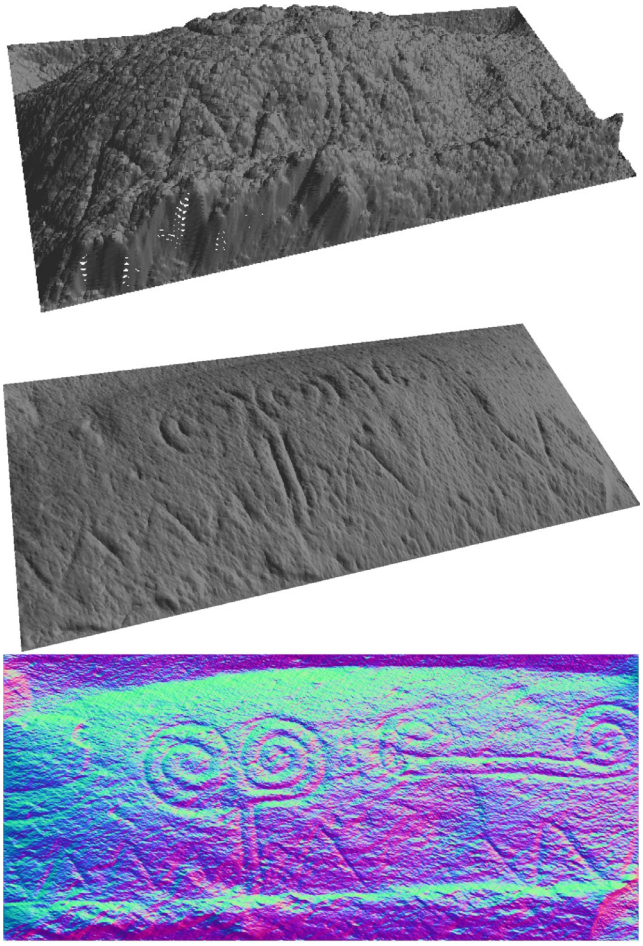

Fig. 8. Perspective view of the reconstruction of the first engraving obtained by the red channel of the dataset (top picture), compared to the one produced by the blue channel (center picture); the bottom picture is the normal map corresponding to the red channel.

Fig. 9. Engraving found in *Domus de Janas di Tomba Branca*, Cheremule, Italy.

The second engraving is found in the *Domus de Janas di Tomba Branca*, Cheremule, Italy; see Fig. 9. The dataset is composed of 13 images, 4 of them reported in Fig. 10. To determine the color matrix to be used for reconstructing the shape, this time we use the first indicator ρ_1. After dataset reduction, we obtain the following results:

$$\rho_1(M_r) = 1.9799,$$
$$\rho_1(M_g) = 2.0147,$$
$$\rho_1(M_b) = 2.0327.$$

Fig. 10. Four of the 13 images from the second dataset, each obtained under different lighting conditions.

In this case, the red channel turns out to be the best choice. The reconstructed 3D surface is reported in Fig. 11, where the complete reconstruction, including shape and albedo, is displayed at the top, followed by the normal map and the pure shape without the albedo. Adopting the indicator ρ_2 leads in this case to acceptable but slightly less accurate results.

5. Discussion and conclusions

A comparison of the 3D color reconstructions reported in Figs. 7 and 11 to the original pictures of the engravings in Figs. 1 and 9, demonstrates that the digital models are very good representations of the observations.

Such digital surfaces have the obvious advantage that they provide geometric information about the engravings, as it is clear from the shape views in Figs. 7 and 11, obtained by removing the albedo information. They can be easily manipulated using mesh visualization software, which allows to rotate or enlarge them, and modify the lighting to enhance details. They can be converted to files suitable for 3D printing and be the starting point for further processing, for example for automatic extraction of glyphs.

It is also remarkable to notice that when the albedo is removed from the model in Fig. 11, one can clearly observe the carvings present on the rock surface, which are almost invisible in the original picture and are hardly observable *in situ* too. So the simple albedo removal is a powerful tool to visualize engravings which may not be easily studied at the excavation site.

In principle, a geometric reconstruction of rock art can be obtained by a laser scanner, but these devices are usually much more expensive than a good digital camera, and require trained personnel for their use. Moreover, for the moment, only few laser scanners provide color information for the observed object, and they are very expensive.

Photometric stereo involves a simple data collection technique, but has the inconvenience to heavily rely on the mathematical techniques adopted for data processing, thus providing a challenging environment for research in applied mathematics.

The technique for processing color pictures of engravings presented in this paper is promising, but it requires further development. Firstly, the method is not fully autonomous, as the two ideality measures ρ_1 and ρ_2 often produce different results. The experimental results presented here were produced by selecting the index ρ_k to be used on the basis of a visual inspection of the results. So, for the moment they do not lead to a fully automatic procedure and only constitute a support for supervised research

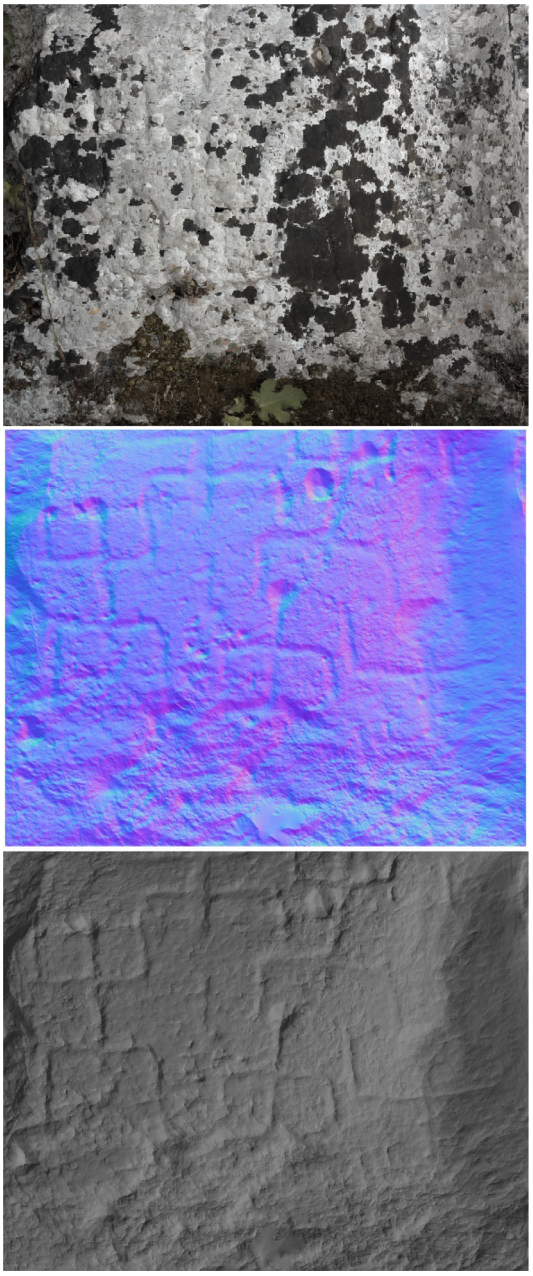

Fig. 11. Reconstruction of the second engraving obtained by the red channel of the dataset: complete color reconstruction (top picture), normal map (center picture), and pure shape without the albedo (bottom picture).

activity. An integration of the two quality measures to obtain an effective algorithm is one of our aim.

Another interesting point is that here we are processing each color independently of the others, while it would be preferable to determine the shape and the color components of the albedo solving a single integrated problem. Unfortunately, this approach seems to lead to a nonlinear large-scale problem, which we are currently studying.

Acknowledgments

The research of FP and GR is partially supported by the PRIN 2022 project “Inverse Problems in the Imaging Sciences (IPIS)” (2022ANC8HL) and by Fondazione di Sardegna, Progetto biennale bando 2021, “Computational Methods and Networks in Civil En-

gineering (COMANCHE)". EC and GR acknowledges partial support from the PRIN-PNRR 2022 project "AQuAInt - Approximation and Quadrature for Applicative Integral Models" (P20229RMLB). EC, FP, and GR are members of the GNCS group of INdAM and are partially supported by INdAM-GNCS 2024 Project "Algebra lineare numerica per problemi di grandi dimensioni: aspetti teorici e applicazioni" (CUP_E53C23001670001). FP gratefully acknowledges OGS and CINECA under HPC-TRES program award number 2024-02.

References

[1] G. Tanda, Le Domus de Janas Decorate con Motivi Scolpiti. Volume 1, Edizioni Condaghes, Cagliari, Italy, 2015.
[2] R.J. Woodham, Photometric method for determining surface orientation from multiple images, Opt. Eng. 19 (1) (1980) 139–144.
[3] R. Dessí, C. Mannu, G. Rodriguez, G. Tanda, M. Vanzi, Recent improvements in photometric stereo for rock art 3D imaging, Digit. Appl. Archaeol. Cult. Heritage (DAACH) 2 (2015) 132–139.
[4] M. Vanzi, P.E. Bagnoli, C. Mannu, G. Rodriguez, Photometric stereo 3D visualizations of rock-art panels, bas-reliefs, and graffiti, in: S. Campana, R. Scopigno, G. Carpentiero, M. Cirillo (Eds.), CAA2015 Keep the Revolution Going, Proceedings of the 43rd Annual Conference on Computer Applications and Quantitative Methods in Archaeology, Archaeopress Archaeology, Oxford, U.K., 2016, pp. 1059–1065. ISBN: 978-1-78491-337-3, 978-1-78491-338-0 (e-Pdf)
[5] J. Mélou, A. Laurent, C. Fritz, J.-D. Durou, 3D digitization of heritage: photometric stereo can help, in: ISPRS-International Archives of the Photogrammetry, Remote Sensing and Spatial Information Sciences, 48, 2022, pp. 145–152.
[6] M. Díaz-Guardamino, L.G. Sanjuán, D. Wheatley, V.R. Zamora, Rti and the study of engraved rock art: a re-examination of the Iberian south-western stelae of Setefilla and Almadén de la Plata 2 (seville, spain), Digit. Appl. Archaeol. Cult. Heritage (DAACH) 2 (2–3) (2015) 41–54.
[7] D. Miyazaki, K. Hara, K. Ikeuchi, Median photometric stereo as applied to the Segonko Tumulus and museum objects, Int. J. Comput. Vis. 86 (2010) 229–242.
[8] K. Ikeuchi, T. Morimoto, M. Kamakura, N. Kuchitsu, K. Kawano, T. Ikeda, Kyushu decorative tumuli project: from e-heritage to cyber-archaeology, Int. J. Comput. Vis. 130 (7) (2022) 1609–1626.
[9] A. Concas, R. Dessí, C. Fenu, G. Rodriguez, M. Vanzi, Identifying the lights position in photometric stereo under unknown lighting, in: 2021 21st International Conference on Computational Science and Its Applications (ICCSA), 2021, pp. 10–20. Cagliari, Italy
[10] Y. Quéau, B. Durix, T. Wu, D. Cremers, F. Lauze, J.-D. Durou, Led-based photometric stereo: modeling, calibration and numerical solution, J. Math. Imaging Vis. 60 (2018) 313–340.
[11] H. Guo, Z. Mo, B. Shi, F. Lu, S.-K. Yeung, P. Tan, Y. Matsushita, Patch-based uncalibrated photometric stereo under natural illumination, IEEE Trans. Pattern Anal. Mach. Intell. 44 (11) (2021) 7809–7823.
[12] G. Chen, K. Han, B. Shi, Y. Matsushita, K.-Y.K. Wong, Self-calibrating deep photometric stereo networks, in: Proceedings of the IEEE/CVF Conference on Computer Vision and Pattern Recognition, 2019, pp. 8739–8747.
[13] S. Ikehata, Scalable, detailed and mask-free universal photometric stereo, in: Proceedings of the IEEE/CVF Conference on Computer Vision and Pattern Recognition, 2023, pp. 13198–13207.
[14] H. Hayakawa, Photometric stereo under a light source with arbitrary motion, J. Opt. Soc. Am. A-Opt. Image Sci. Vis. 11 (11) (1994) 3079–3089.
[15] G. Radow, G. Rodriguez, A. Mansouri Yarahmadi, M. Breuß, Photometric stereo with non-Lambertian preprocessing and Hayakawa lighting estimation for highly detailed shape reconstruction, in: E. Cristiani, M. Falcone, S. Tozza (Eds.), Mathematical Methods for Object Reconstruction: from 3D Vision to 3D Printing, Springer INdAM Series, 54, Springer, Singapore, 2023, pp. 35–56.
[16] S. Ikehata, D. Wipf, Y. Matsushita, K. Aizawa, Robust photometric stereo using sparse regression, in: 2012 IEEE Conference on Computer Vision and Pattern Recognition, IEEE, 2012, pp. 318–325.
[17] F. Logothetis, I. Budvytis, R. Mecca, R. Cipolla, PX-NET: simple and efficient pixel-wise training of photometric stereo networks, in: Proceedings of the IEEE/CVF International Conference on Computer Vision, 2021, pp. 12757–12766.
[18] Y. Ju, B. Shi, M. Jian, L. Qi, J. Dong, K.-M. Lam, NormAttention-PSN: a high-frequency region enhanced photometric stereo network with normalized attention, Int. J. Comput. Vis. 130 (12) (2022) 3014–3034.
[19] L. Wu, A. Ganesh, B. Shi, Y. Matsushita, Y. Wang, Y. Ma, Robust photometric stereo via low-rank matrix completion and recovery, in: Computer Vision–ACCV 2010: 10th Asian Conference on Computer Vision, Queenstown, New Zealand, November 8–12, 2010, Revised Selected Papers, Part III 10, Springer, 2011, pp. 703–717.
[20] E. Crabu, F. Pes, G. Rodriguez, G. Tanda, Ascertaining the ideality of photometric stereo datasets under unknown lighting, Algorithms 16 (2023). 375 (15 pages)
[21] P.H. Christensen, L.G. Shapiro, Three-dimensional shape from color photometric stereo, Int. J. Comput. Vis. 13 (2) (1994) 213–227.
[22] S. Barsky, M. Petrou, Colour photometric stereo: Simultaneous reconstruction of local gradient and colour of rough textured surfaces, in: Proceedings Eighth IEEE International Conference on Computer Vision. ICCV 2001, 2, IEEE, 2001, pp. 600–605.
[23] O. Ikeda, Y. Duan, Color photometric stereo for albedo and shape reconstruction, in: 2008 IEEE Workshop on Applications of Computer Vision, IEEE, 2008, pp. 1–6.
[24] M.S. Drew, Shape From Color, Technical Report, Simon Fraser University, School of Computing Science, Vancouver, Canada, 1992.
[25] R. Mecca, M. Falcone, Uniqueness and approximation of a photometric shape-from-shading model, SIAM J. Imaging Sci. 6 (2013) 616–659.
[26] X. Cao, H. Santo, B. Shi, F. Okura, Y. Matsushita, Bilateral normal integration, in: European Conference on Computer Vision, Springer, 2022, pp. 552–567.
[27] G.H. Golub, C.F. Van Loan, Matrix Computations, third ed., The John Hopkins University Press, Baltimore, 1996.
[28] P.N. Belhumeur, D.J. Kriegman, A.L. Yuille, The bas-relief ambiguity, Int. J. Comput. Vis. 35 (1) (1999) 33–44.
[29] Å. Björck, Numerical Methods for Least Squares Problems, SIAM, Philadelphia, 1996.
[30] F. Pes, G. Rodriguez, The minimal-norm Gauss-Newton method and some of its regularized variants, Electron. Trans. Numer. Anal. 53 (2020) 459–480.
[31] F. Pes, G. Rodriguez, A doubly relaxed minimal-norm Gauss–Newton method for underdetermined nonlinear least-squares problems, Appl. Numer. Math. 171 (2022) 233–248.
[32] E. Crabu, G. Rodriguez, A synthetic dataset generator for photometric stereo, 2024. Submitted. Software available at https://bugs.unica.it/cana/software.html.